Extracting Electrons from Delocalized Excitons by Flattening the Energetic Pathway for Charge Separation

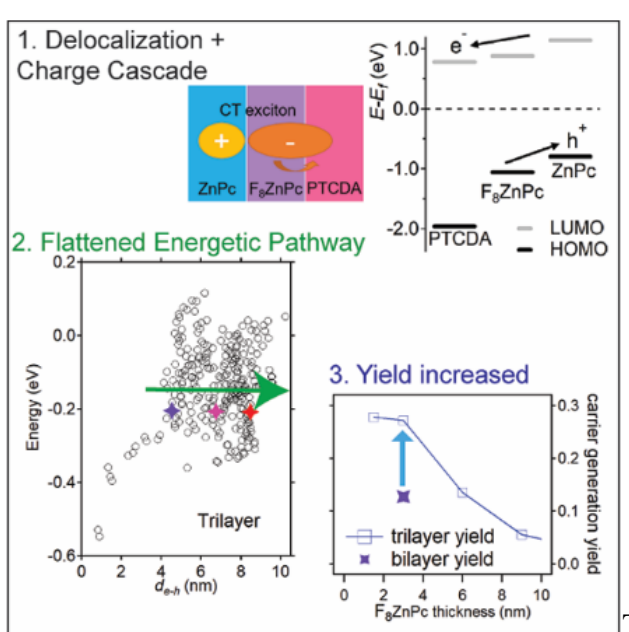
Shanika Wanigasekara, Bhupal Kattel, Fatimah Rudayni, Wai-Lun Chan*

Department of Physics and Astronomy, University of Kansas, Lawrence, KS 66045, USA

Abstract:

At organic donor-acceptor (D-A) interfaces, electron and hole are bound together to form charge transfer (CT) excitons. The electron and hole wavefunctions in these CT excitons can spatially delocalize. The electron delocalization opens up possibilities of extracting free charges from bound excitons by manipulating the potential energy landscape on the nanoscale. Using a prototype trilayer structure that has a cascade band structure, we show that the yield of charge separation can be doubled as compared to the bilayer counterpart when the thickness of the intermediate layer is around 3 nm. This thickness coincides with the electron delocalization size of CT excitons typically found in these organic films. Tight-binding calculation for the CT states in the trilayer structure further demonstrates that electron delocalization, together with the energy level cascade, can effectively flatten the energetic pathway for charge separation. Hence, it is possible to add nanometer-thick layers between the donor and the acceptor to significantly enhance the charge separation yield.

*Email: wlchan@ku.edu



TOC Figure

Extracting free charge carriers from bound excitons has been a bottleneck process for the photo-to-electrical conversion in organic and nano-materials. At a typical organic donor-acceptor (D-A) interface, electron and hole are bound together to form the so-called charge transfer (CT) exciton. The relatively large binding energy of these CT excitons increases the likelihood of recombination before the CT exciton can dissociate, which limits the photo-to-electrical conversion yield. Tightly-bound excitons can also be found in other low dimensional materials such as monolayer transition metal dichalcogenide crystals (TMDC)⁷⁻⁸ and nanocrystals. Hence, developing strategies to separate excitons into free charges is crucial for employing these materials in light harvesting applications. It is proposed that hot CT excitons, with excess vibrational or electronic energies acquired from the energy offset at the D-A interface, can facilitate the separation of CT excitons into free charges. However, the lifetime of these hot CT excitons is extremely short and they tend to lose their excess energy within a few ps. In order to extract free charges from hot CT excitons before they relax into tightly-bound states, electron and hole need to be separated from each other on a sub-ps timescale, which can be a challenging task.

CT exciton dissociation, or often referred to as charge separation (CS), would be facilitated by controlling the potential energy landscape near the D-A interface such that electron and hole can be funneled to sites that are close to, but are slightly away from the D-A interface. Indeed, it has been proposed that imperfections near the interface introduced by molecular mixing ¹⁹⁻²³ or disorder ²⁴ would promote CS. Furthermore, it is known that electron and hole within a hot CT exciton can be spatially delocalized with a delocalization size on the order of a few nm. ^{13-15, 18, 25} The electron delocalization, together with nanoscale-potential energy landscape design, can open up new possibilities of using multilayer structures to extract charges from bound CT excitons. For example, a charge cascade structure shows in Fig. 1a can achieve such goal if the thickness of the

middle layer is on the order of the electron delocalization size. Electron delocalization allows the two interfaces to couple coherently, which assists the separation of bound CT excitons formed at either of the interfaces. CS across an intermediate layer *via* interlayer electronic delocalization has been demonstrated in TMDC multilayer structures. For organic materials, although charge cascade structures have been shown to increase the photovoltaic efficiency, 27-31 the efficiency-increase is often attributed to a reduction in the electron-hole recombination after the CS. Because the increase in the photocurrent can also be attributed to the enhancement in the initial CS yield, steady-state device measurements often unable to detangle the contribution from each of the two processes. Hence, it remains unclear whether a cascade structure, with its thickness matching the electron delocalization size, can enhance the initial separation yield of delocalized CT excitons.

Here, we use our recently developed time-resolved graphene field effect transistor (TR-GFET) technique to probe the dynamics and yield of free carrier generation in prototype trilayer structures consisting of vacuum-deposited small molecule films. Previously, our time-resolved photoemission studies found that hot CT excitons in these films have an electron delocalization size of ~3–5 nm.^{18, 32-34} Here, the TR-GFET technique³⁵⁻³⁶ selectively probes free charges generated by the CS process. By probing the concentration of separated charges as a function of time, we can independently measure the initial CS yield and the recombination rate of separated carriers, and distinguish effects from each of those processes on the overall photocurrent. We find that the initial CS yield is doubled in a trilayer sample as compared to a bilayer sample with a similar optical density, when the thickness of the cascade structure matches the electron delocalization size of the CT exciton. Our tight-binding model further shows that electron delocalization across the cascade structure flattens the energetic pathway for CS, which reduces the energy barrier for CS, and would explain the increase in the initial CS yield observed in the

experiment. Our study demonstrates that an artificially tailored multilayer structure can be used to extract charge carriers from bound excitons *via* electron delocalization.

A trilayer structure consists of 3,4,9,10-perylenetetracarboxylic dianhydride (PTCDA), fluorinated zinc phthalocyanine (F_8ZnPc) and ZnPc, which are deposited consecutively on a graphene substrate in an ultrahigh vacuum (UHV) chamber. These molecules are expected to have a face-on orientation^{33, 37} with the π -stacking direction lies along the surface normal direction. Detailed sample preparation procedures can be found in the method section. The energy level diagram of our trilayer structure is shown in Fig. 1a. The highest occupied molecular orbital (HOMO) onsets of the three molecules are determined from a series of ultraviolet photoemission spectroscopy (UPS) spectra which are shown in Fig. 1b. The energy is reference with respect to the Fermi level (E_f). The lowest unoccupied molecular orbital (LUMO) position in Fig. 1a is determined by using the reported HOMO-LUMO gaps (onset-to-onset) of the three molecules.³⁸⁻³⁹ The multilayer structure forms a charge cascade which can funnel electron and hole into the PTCDA and ZnPc layers, respectively (Fig. 1a).

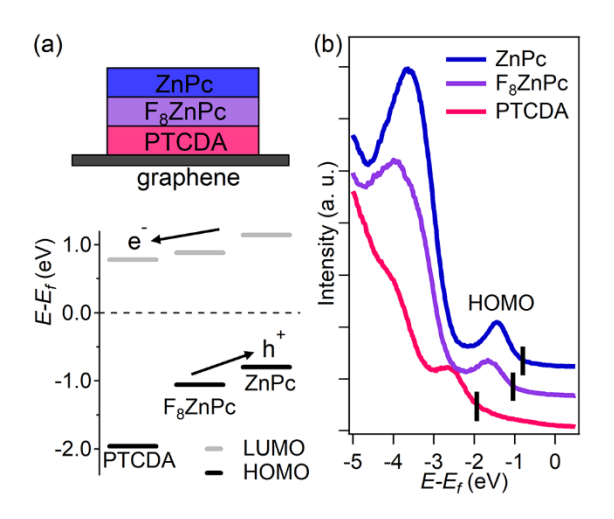


Fig. 1. a) A schematic diagram shows a trilayer film deposited on graphene and its energy level diagram. b) UPS spectra that are used for determining the HOMO energy levels in (a). The three samples have the following thicknesses: (red) 5-nm PTCDA; (purple) 5-nm F₈ZnPc/5-nm PTCDA; (blue) 2-nm ZnPc/5-nm F₈ZnPc/5-nm PTCDA.

Figure 2a illustrates how the GFET sensor is used to measure the CS dynamics from the trilayer structure. In the TR-GFET experiment, the ZnPc and F₈ZnPc layers are selectively excited by a 700-nm, 25-fs laser pulses. After the consecutive CT and CS processes, free holes remain trapped in the ZnPc layer while free electrons transport to the PTCDA layer and, subsequently, inject into graphene through the charge cascade structure. The trapped holes in the topmost ZnPc layer induce an equal number of electrons in the graphene by capacitive coupling as in a parallel plate capacitor. As a result, the graphene becomes n-doped. This n-doping produces a measureable change in the graphene's conductivity⁴⁰⁻⁴¹ because of the low density of state of graphene near the Dirac point. The change in the graphene's channel resistance ($\Delta R_G/R_G$), which is captured by a 200 MHz oscilloscope,^{35, 42} provides a direct measurement of the number of separated charges as a function of time.

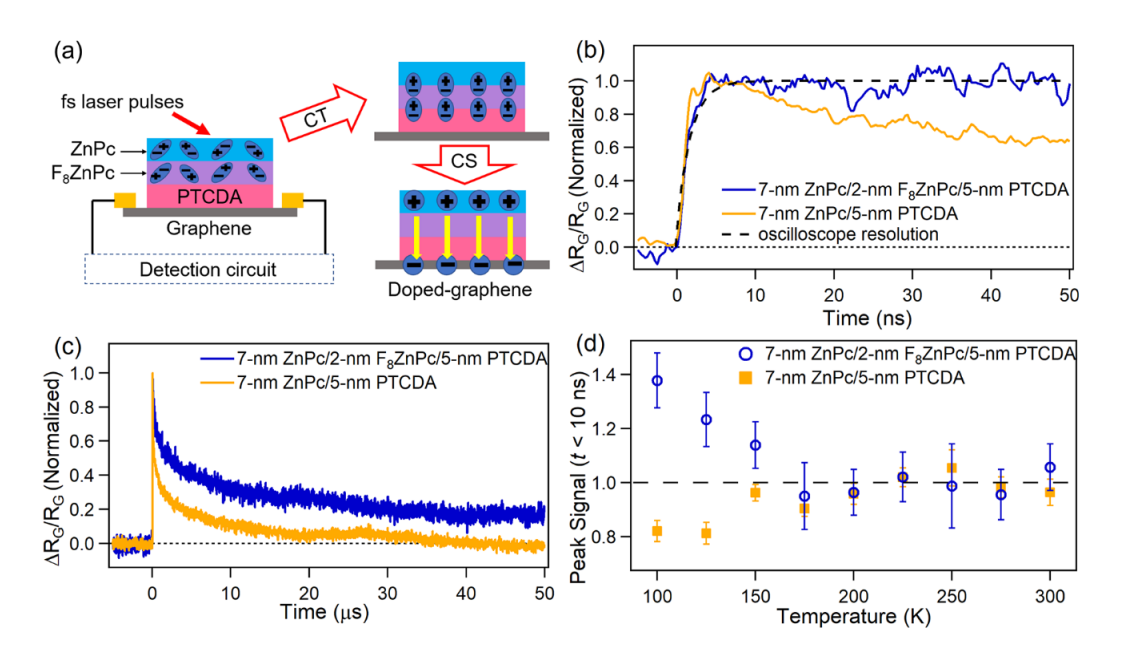


Figure 2. a) A schematic diagram shows how the free carriers generated by the CS can be detected by the GFET sensor. The resistance change ($\Delta R_G/R_G$) of the doped graphene is measured by an oscilloscope, which is proportional to the amount of separated carriers. (b) The normalized $\Delta R_G/R_G$ signal for bilayer ZnPc/PTCDA and trilayer ZnPc/F₈ZnPc/PTCDA samples on a short timescale; and (c) a longer timescale. (d) The signal amplitude near time zero, which is proportional to the initial CS yield, as a function of temperature.

Figures 2b and 2c show the normalized $\Delta R_G/R_G$ signal of bilayer 7-nm ZnPc/5-nm PTCDA, and trilayer 7-nm ZnPc/2-nm F₈ZnPc/5-nm PTCDA samples collected on two different timescales. In Fig. 2b, the signal rise time represents the time needed for generating free electron-hole pairs. For comparison, the instrumental rise time of the oscilloscope is shown as the dashed line. The signal rise time is limited by the time-resolution of our oscilloscope (~ 1 ns) for both samples. The fast rise time is reasonable because the sample thickness is comparable to both the exciton delocalization size 43-44 and the electron delocalization size of the CT exciton 18, 33, 36 that we previously found in these thin films. Hence, the whole charge generation process is not limited by the slow incoherent diffusion of either excitons or free charges. Indeed, as a reference, the signal rise time increases if we increase the PTCDA's thickness to 15 nm (supporting information, Fig. S1). Here, we will focus on thinner samples such that the CT and CS processes, instead of incoherent diffusion, are probed. Moreover, the dynamics on the longer timescale (Fig. 2c) probes the recombination kinetics of the electron-hole pair. The electron-hole recombination in the trilayer sample is significantly slower than that of the bilayer sample as shown by the longer signal lifetime. This behavior is expected because the middle F₈ZnPc layer spatially separates the electron and hole, which reduces the electron-hole recombination.

In order to understand the CS mechanism, the initial signal amplitude (at $t \sim 4 - 14$ ns) as a function of temperature is measured. Figure 2d shows the signal amplitude of the bilayer and trilayer samples at different temperatures. For comparison, the amplitude is normalized with the amplitude at the room temperature. Although both samples show a weak temperature dependence, the trend is very different. For the bilayer sample, the signal amplitude decreases slightly with the temperature. In this sample, both PTCDA and ZnPc molecules have a face-on orientation.³³ Our previous work has shown that the entropic driving force facilitates CS at this orientation, which

results in the weak temperature dependence.³²⁻³³ By contrast, for the trilayer sample, the signal amplitude *increases* at lower temperatures. This is rather surprising because the CS is an enthalpy uphill process, which should be suppressed at lower temperatures. On the other hand, the electron delocalization size should increase at lower temperatures because of the reduction in dynamical disorders. Therefore, if the CS is facilitated by electron delocalization, the yield of such channel should increase at lower temperatures. Hence, the increase in the CS yield at lower temperatures is consistent with the proposed delocalization-assisted CS in the trilayer sample.

We further measure the absolute number of separated carriers in the trilayer sample as a function of the intermediate layer, i.e. F_8ZnPc , thickness. For this purpose, back-gated samples with the graphene transferred on SiO_2 (300 nm)/Si instead of glass were used. By applying a back gate voltage (V_g) to the highly-doped Si substrate, the graphene can be doped electrically⁴⁵⁻⁴⁶ and the change in the resistance as a function of V_g can be obtained. Because the number of carriers induced by the electrical gating can be determined simply by using the equation of a parallel plate capacitor, the V_g -dependent measurement can be used to calibrate the response of a graphene sensor originated from the doping. An example of such data is shown in Fig. 3a.

In this measurement, the sample was illuminated with fs laser pulses (700 nm) and the graphene's resistance was determined before (t < 0 ns; corresponding to the dark condition), and immediately after the fs laser pulse excites the sample ($t \approx 10$ ns; corresponding to the light condition). This early time signal represents the amount of free charges generated from the initial dissociation of CT excitons before the recombination of these separated carriers occurs. We note that measurements obtained from samples on SiO₂/Si systematically underestimate the resistance-change near time zero because of the much larger RC response time of back-gated samples (see supporting information). Therefore, the resistance change at $t \approx 10$ ns is corrected by a factor that

is determined by comparing time traces obtained from a pair of samples with the same thicknesses made on glass and on SiO₂/Si (Fig. S2). The dark and light resistance at various V_g is plotted in Fig. 3a. The shift of the whole curve to the left under the light indicates that optical excitation dopes the graphene with electrons. The number of the separated electrons N can be related to the voltage shift (ΔV_g) by:³⁵

$$N = \Delta V_g \frac{\kappa \varepsilon_0 A}{d} \frac{1}{e},\tag{1}$$

where κ and d are the dielectric constant and the thickness of SiO₂ respectively, ϵ_0 is the vacuum permittivity, A is the area of the graphene channel and e is the electron charge.

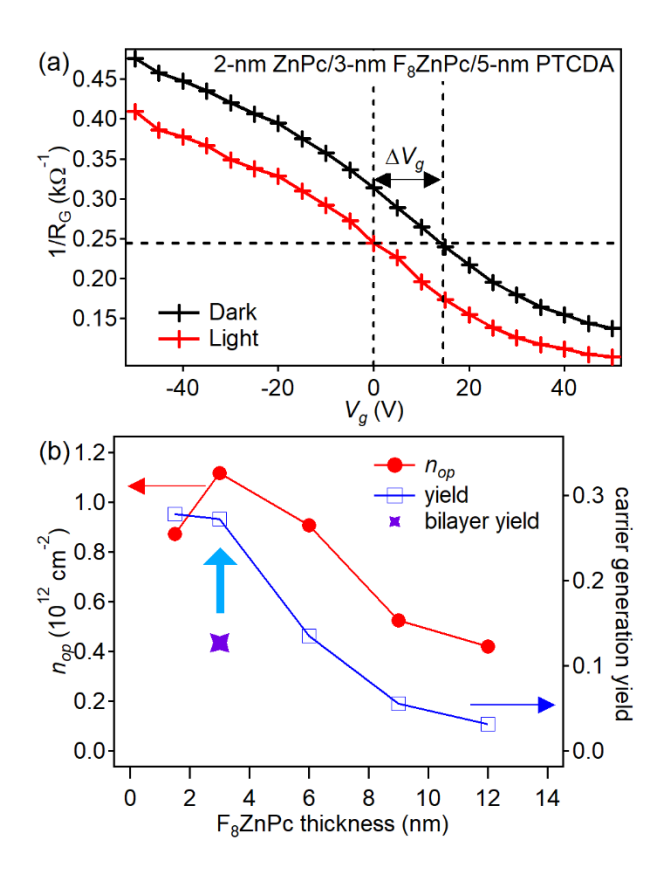


Figure 3. (a) The inverse of the graphene's channel resistance as a function of the gate voltage V_g for the 2-nm ZnPc/3-nm F₈ZnPc/5-nm PTCDA trilayer sample. Optical excitation results in a horizontal shift of the curve (ΔV_g), which can be used to calculate the amount of separated charges N using Eq. (1). (b) The red curve shows the density of the separated charge as a function of F₈ZnPc thickness for trilayer samples. The thicknesses of ZnPc and PTCDA are fixed at 2 nm and 5 nm, respectively. The blue curve represents the quantum yield of CS. For comparison, the same measurement is done for a 5-nm ZnPc/5-nm PTCDA bilayer sample. The CS yield of the bilayer

sample (purple star) is compared to that of the 2-nm ZnPc/3-nm F₈ZnPc/5-nm PTCDA trilayer sample, which has a nearly identical optical density. The CS yield of the trilayer sample is doubled compared to that of the bilayer sample.

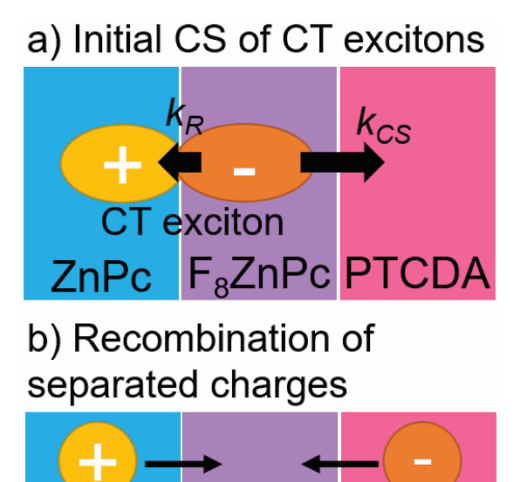
Figure 3b shows the average density of the separated carriers ($n_{op} = N/A$) for trilayer samples as a function of the F₈ZnPc thickness. The thickness of the ZnPc and PTCDA layers are fixed at 2-nm and 5-nm, respectively. The number of separated carriers (red curve) increases at small thicknesses because of the increase in the light absorber (F₈ZnPc) thickness. It peaks at a F₈ZnPc-thickness of around 3 nm. When the thickness of the F₈ZnPc layer is further increased, n_{op} decreases. The decrease in n_{op} can be attributed to the thickness of the F₈ZnPc layer being larger than the electron delocalization size, which was found to be around 4 nm in our samples. ^{18, 32-33, 36} When the intermediate layer thickness is larger than the electron delocalization size, the two interfaces (ZnPc/F₈ZnPc and F₈ZnPc/PTCDA) are decoupled and delocalization can no longer assist the separation of the CT exciton. Moreover, charges need to diffuse across the thicker intermediate layer through incoherent hopping, which further lowers the overall CS yield.

In our experiment, a laser wavelength of 700 nm (1.78 eV) is used. This photon energy is smaller than the optical gap of PTCDA. Hence, the optical absorption of the PTCDA layer is much weaker than that of ZnPc and F_8 ZnPc layers. We have estimated the optical absorption in ZnPc and F_8 ZnPc by a transfer matrix optical model. 47-48 that accounts for the multilayer interference effects (see supporting information). This allows us to determine the quantum yield of CS for each sample. The yield as a function of the F_8 ZnPc-thickness is shown as the blue curve in Fig. 3b (right axis). We note that the yield is relatively low ($\sim 10-30$ %) because our sample is at the open-circuit condition, i.e. the carriers are not swept out from the active layer, but opposite charges built up on top and bottom faces of the multilayer stack can stop further CS. The yield is the highest for F_8 ZnPc-thicknesses ≤ 3 nm and it decreases at larger thicknesses. For comparison, the result for

the bilayer 5-nm ZnPc/5-nm PTCDA sample is shown on the plot as the purple star. The bilayer 5-nm ZnPc/5-nm PTCDA sample is compared with the 2 nm-ZnPc/3-nm F₈ZnPc/5-nm PTCDA sample because they have similar optical densities (ZnPc and F₈ZnPc have similar optical absorption cross-sections⁴⁹). The comparison shows that the addition of the F₈ZnPc interlayer increases the yield from ~ 12.7 % (bilayer) to ~ 27.2 % (trilayer) (the vertical arrow in Fig. 3b). The doubling of the CS yield demonstrates that the use a charge cascade structure can significantly enhance the CS yield when the thickness of the intermediate layer is smaller than or close to the electron delocalization size.

Before we continue with our discussion, it is worthwhile to recapture the result from our previous work on the ZnPc/F₈ZnPc interface, in which the fs- and ps- dynamics of the CT exciton is probed by time-resolved two photon photoemission spectroscopy (TR-TPPE).^{32, 33} At the ZnPc/F₈ZnPc interface, a mixture of bound CT excitons and loosely-bound electron-hole pairs (these two states are labelled as CT and CS states in Ref. [32, 33]) is formed in ~ 10 ps after the photoexcitation. This CT/CS mixture recombines with an exponential decay time of 830 ps (Fig. S4 in the supporting information). Moreover, the spectral shape of this CT/CS peak in the photoemission spectrum does not change much for t > 50 ps while the overall population decays.³²⁻³³ Hence, this CT/CS mixture is stable and does not undergo significant energy relaxation or trapping prior to its recombination. For the TR-GFET experiment, the electron can be extracted from this CT/CS mixture throughout its ~ 1 ns lifetime whenever the electron reaches the graphene layer *via* stochastic motions. In Fig. 3b, the initial CS yield is calculated from the TR-GFET signal in the first few ns after photoexcitation. Considering that the signal decay in the first 10 ns is small (< 10 %, see Fig. 2b), the yield shown in Fig. 3b essentially represents the initial CS yield of this

CT/CS mixture. Here, we refine our definition of the "initial CS yield" to as the yield for successful electron extraction from the CT/CS mixture prior to the CT exciton recombination.



F₈ZnPc PTCI

Figure 4. Schematics show (a) the initial CS process of the CT exciton and (b) the recombination of separated charge carriers. The F_8 ZnPc can both increase the initial CS yield and reduce the recombination of separated charges. In our measurement, the former leads to the increase in the signal amplitude in early times ($\sim 1-10$ ns) while the latter leads to a longer signal lifetime.

Typically, in a cascade structure, two mechanisms can increase the overall free carrier generation yield and the resultant photocurrent. First, the initial CS yield of the CT exciton (illustrated in Fig. 4a) can increase due to the presence of the cascade structure. The change in the local energy landscape resulting from the middle layer can increase the CS rate (k_{CS}) relative to the recombination rate (k_R) of the CT exciton, which increases the initial CS yield. As mentioned above, the increase in the initial CS yield leads to the increase in the signal amplitude in early times (a few ns) in our time-resolved experiment. Second, the middle layer can act as a barrier to prevent the recombination of separated carriers (Fig. 4b), which can increase the photocurrent in typical steady-state measurements as well. However, in our time-resolved measurement, the reduced recombination of separated carriers is manifested as an increase in the signal lifetime (see Fig. 2c). Hence, the data shown in Fig. 3, which is obtained from the signal amplitude in the first

few ns after the photoexcitation, does not capture the reduced recombination of the separated electrons and holes as shown in Fig. 4b. In the discussion below, we will focus on how the cascade structure and the electron delocalization can potentially enhance the initial CS yield.

In Fig. 3, it can be seen that the CS yield decreases when the middle layer becomes too thick (e.g., the yield drops significantly at thickness ≥ 6 nm). Hence, the trilayer structure is effective only when the two interfaces are close to each other. From our previous time-resolved photoemission experiments, $^{18, 33-34}$ we know that the electron delocalization size of CT excitons in these organic films is in the range of 3-5 nm. The optimal thickness of the middle (F_8 ZnPc) layer coincides with the electron delocalization size of CT excitons. Therefore, we hypothesize that the electron delocalization, together with the cascade structure, can enhance the initial CS yield. To understand how electron delocalization would increase the initial CS yield, we model energies of delocalized CT and CS states in the trilayer structure. The energy difference between CT and CS states corresponds to the energy barrier of the CS process. A reduction in this energy barrier can significantly increase the k_{CS} shown in Fig. 4a.

To determine the CT and CS state energies, we first note that the strong intermolecular coupling along the π -stacking direction produces a manifold of CT-CS states with spatially delocalized electron and hole.^{12, 25} States within this manifold can have different energies (*E*) and electron-hole separations (d_{e-h}). The variation in the local energy landscape introduced by the charge cascade structure can affect the E- d_{e-h} relationship, which in turn determines the energetic pathway for CS. We model *E* and d_{e-h} of the manifold of CT/CS states in a 1-D molecular chain using a generic tight-binding model³²⁻³³ that consists of three layers (donor, acceptor-1 and acceptor-2). The intermolecular distance is set to be 0.4 nm. In this model, the hole is located at the donor (ZnPc) layer, while the electron can delocalize across the acceptor-1 (F₈ZnPc) and the

acceptor-2 (PTCDA) layer. Under the site representation, a CT-CS state is described by a two-body wavefunction $|i,j\rangle$, where i and j are indexes representing the positions of electron and hole, respectively. The eigenstates are then found by diagonalization the tight-binding Hamiltonian:

$$H = \sum_{i}^{N} \sum_{j}^{M} V_{c}(i,j)|i,j\rangle\langle i,j| - \sum_{i}^{N} \sum_{j}^{M} E_{off}\delta(j-j_{ac2})|i,j\rangle\langle i,j| + \sum_{j}^{M} \sum_{i,n,i\neq n}^{N} J_{el}(n,i)|n,j\rangle\langle i,j| + \sum_{i}^{N} \sum_{j,m,i\neq m}^{M} J_{h}(m,j)|i,m\rangle\langle i,j|$$

In this equation, the function $V_c(i, j)$ represents the Coulomb interaction between the electron and hole. Furthermore, if the electron is located on an acceptor-2 site (j_{ac2}) , the energy of $|i,j\rangle$ is reduced by the LUMO offset (E_{off}) found at the F₈ZnPc/PTCDA interface. E_{off} is set to be 0.1 eV based on our estimation (Fig. 1). The term $J_{el}(n, i)$ is the electron transfer integral between site n and site i and $J_h(m, j)$ is the hole transfer integral between site m and site j. Here, we only consider the electronic coupling between nearest-neighbor sites. The eigenenergy (E) represents the sum of the Coulomb binding energy, the energy stabilization due to the cascade structure, and the energy bandwidth resulting from the nearest-neighbor electronic coupling. We model the energy and the probability distribution of eigenstates for a trilayer (donor/acceptor-1/acceptor-2 with thicknesses of 5.2-nm/3.2-nm/5.2-nm) and a bilayer structure (donor/acceptor with thicknesses of 5.2-nm/8.4-nm). For the bilayer structure, E_{off} is set to be zero.

Figure 5a and b show the distribution of eigenstates in the E- d_{e-h} space. Each dot represents an eigenstate. A distinct difference between the two distributions can be seen. For the bilayer sample (Fig. 5a), E increases continuously with d_{e-h} , which can be understood as a continuous reduction in the Coulomb binding energy as d_{e-h} increases. On the other hand, for the trilayer structure, E is insensitive to d_{e-h} for $d_{e-h} > 2$ nm. The energetic pathway for the CS is "flatten" at larger d_{e-h} because the site energy (the 2^{nd} term in Eq. 1) is reduced as the wavefunction spreads from the acceptor-1 layer to the acceptor-2 layer, which compensates the energy increase

originated from a weaken Coulomb interaction (the 1st term in Eq. 1). The flatten energetic pathway allows CS to occur iso-energetically as far as some relative hot CT excitons are initially populated (e.g. the state represented by the purple star in Fig. 5b).

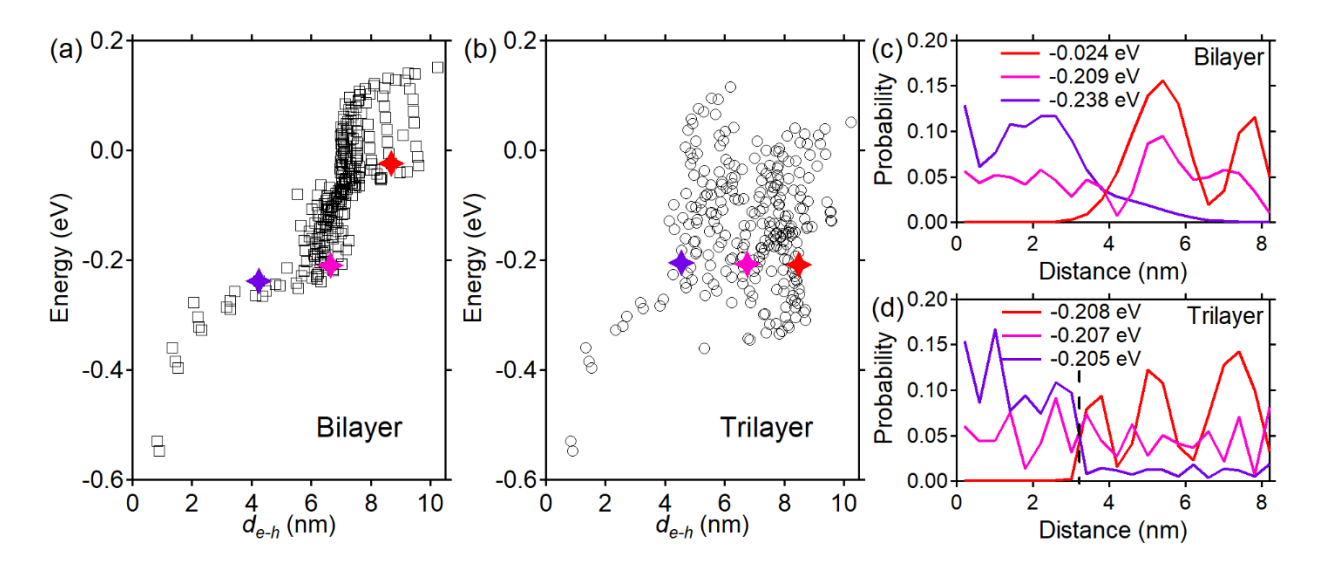


Figure 5: Distribution for the eigenstates in the E- d_{e - $h}$ space for (a) a bilayer sample and (b) a trilayer sample. The thickness for the bilayer and trilayer samples are 5.2-nm (donor)/8.4-nm (acceptor), 5.2-nm (donor)/3.2-nm (acceptor 1)/3.2-nm (acceptor 2), respectively. (c, d) The probability distribution of the electron wavefunction for eigenstates shown as stars in (a) and (b). The energies of these states are shown in the figure legend. The D-A interface is located at the distance equal to zero. For the trilayer sample, the interface between acceptor 1 and acceptor 2 is shown by the vertical dashed line.

To visualize the wavefunction for eigenstates with different d_{e-h} , the probability distribution of the electron for three selected eigenstates (shown as stars in Fig. 5a and 5b) are plotted in Fig. 5c and 5d. The color of the lines in Fig. 5c and 5d is chosen to match the color of the stars shown in Fig. 5a and 5b. The purple states represent hot CT exciton states with the delocalized electron residing near the D-A interface. Typically, these hot CT states are populated initially after the charge transfer occurs at the D-A interface. ^{11, 18} The red states represent CS states in which the electron is separated from the hole. The hot CT state can transition into the CS state *via* intermediate states (magenta states) in which the electron is delocalized across the whole acceptor layer. For the trilayer structure, the three types of states have similar energies, which allows an

iso-energetic CS process. On the other hand, CS states has distinctly higher energies in the bilayer sample, which results in an energy uphill CS process. We note that the energy stabilization effect introduced by the acceptor-2 layer diminishes if the thickness of the middle acceptor-1 layer is larger than the electron delocalization size. For a thick acceptor-1 layer, CS will need to occur *via* an energy uphill process as in the donor/acceptor-1 layers first before the separated electron can migrate into the acceptor-2 layer. In the other word, the two interfaces decouple from each other. We would like to comment that our model does not calculate the time dependent dynamics directly. Moreover, it does not include electron-vibration interactions, which would localize the electron and change the energies of some of those CT/CS states. Therefore, it can only be treated as an illustration on how the electron delocalization would affect the energetic pathway for CS and the initial CS yield.

In summary, we show that in a trilayer charge cascade structure, if the thickness of the intermediate layer matches the electron/hole delocalization size within the CT exciton, the CS yield can be enhanced significantly. In the case of the ZnPc/F₈ZnPc/PTCDA, the CS yield is increased by ~ 100% as compared to the bilayer ZnPc/PTCDA with an equivalent optical thickness. The much larger CS yield at the open circuit condition implies that a smaller internal E-field would be needed to separate the CT exciton if such cascade structure is implemented at the D-A interface in an organic solar cell. The cascade structure can potentially reduce the energy loss contributed by the CT exciton binding, which can in turn improve the open circuit voltage of the solar cell.

METHOD

Sample Preparation - To fabricate the sample, monolayer CVD graphene grown on Cu (purchased from Graphene Supermarket) was transferred either on glass or SiO₂/Si (for back-gated

samples). Before used, these substrates are cleaned by methanol and acetone. The standard wet transfer method with Polymethyl methacrylate (PMMA) stamp was used to transfer the graphene. The transferred graphene was then loaded into a UHV deposition chamber (with a base pressure of 10-9 Torr) for electrode (Ag, ~ 100 nm thick) deposition. A shadow mask was used to define an array of electrodes. Then, a different shadow mask was used to cover the graphene channel. The sample was then sputtered by a 1 keV Ar ion beam so that a 1 mm x 1 mm graphene channel can be patterned between two electrodes. The graphene device was then annealed inside the UHV deposition chamber at 400 °C overnight to remove polymer residues that may remain on the graphene surface. After the annealing, PTCDA (Alfa Aesar, 98%), F₈ZnPc (Luminescence Technology, Taiwan, >99%), and ZnPc (Luminescence Technology, Taiwan, >99%) were deposited on the graphene using thermal evaporation. The deposition rates were kept at 0.3-0.4 Å/minutes for PTCDA, and 0.8-1.0 Å/minutes for F₈ZnPc and ZnPc. The thickness of the film was monitored using a quartz crystal microbalance.

TR-GFET Measurements - The sample was first loaded into a high vacuum cryostat (pressure ~ 10⁻⁶ Torr). It was excited by a femtosecond laser (output from Light Conversion Orpheus-N-2H pumped by Pharos 10 W). The wavelength and the repetition rate were 700 nm and 100 Hz, respectively. Note that the low repetition rate is achieved by using a pulse picker inside the Pharos laser. The duration of each pulse was 25 fs. The pulse energy was around 340 nJ. The full-width-half maxima of the pulse size is 1.2 mm, which roughly covered the whole graphene channel. The graphene channel was connected to a reference resistor and a DC power source in series. The voltage drop across the reference resistor was measured by a 200 MHz oscilloscope (Keysight DSOX2024A). A portion of the laser beam was split from the main beam using a quartz window,

which was directed to a photodiode in order to produce a signal for triggering the measurement.

The final time trace was obtained by averaging 1024 traces obtained from 1024 laser pulses.

UPS Spectroscopy – The UPS measurement was done using the He-I emission line (21.22 eV)

generated from a UV discharge lamp. The kinetic energy of the photoelectrons were measured

using a hemispherical electron analyzer (Phoibos 100, SPECS).

Tight-binding model - A 1-D tight-binding model is used to model the bilayer and trilayer

samples. The Coulomb potential is given by: $V_c(i,j) = -\frac{e^2}{4\pi\kappa\epsilon_0} \frac{1}{r_{i,i}}$, where ϵ_0 is the vacuum

permittivity, κ is the dielectric constant, and $r_{i,j}$ is the distance between site i and site j. A dielectric

constant equal to 3.5 was used, which is a typical value for organic semiconductors. The electron

and hole transfer integral (J_{el}, J_h) between nearest neighbors was set to be 50 meV. This value is

in line with typical values reported for organic crystals. 51-54 At the acceptor 1 and acceptor 2

interface, J_{el} is reduced to 20 meV. The nearest neighbor distance is set to be 4 Å, which is typical

for the intermolecular distance for planar molecules along the π -stacking direction.

ASSOCIATED CONTENT

Supporting Information

Additional TR-GFET data, details for modeling the optical absorption, ps dynamics of CT

excitons

AUTHOR INFORMATION

Corresponding authors:

Wai-Lun Chan – E-mail: wlchan@ku.edu

The authors declare no competing financial interest.

ACKNOWLEDGMENTS

We acknowledge the support by U.S. National Science Foundation, Grant DMR-1351716 and

DMR-2109979. This investigation was also supported by the University of Kansas General

Research Fund allocation #2151080. F.R. acknowledges the support from Jazan University.

17

REFERENCES

- (1) Bredas, J. L.; Norton, J. E.; Cornil, J.; Coropceanu, V. Molecular Understanding of Organic Solar Cells: The Challenges. *Acc. Chem. Res.* **2009**, *42*, 1691-1699.
- (2) Clarke, T. M.; Durrant, J. R. Charge Photogeneration in Organic Solar Cells. *Chem. Rev.* **2010,** *110*, 6736-6767.
- (3) Heeger, A. J. 25th Anniversary Article: Bulk Heterojunction Solar Cells: Understanding the Mechanism of Operation. *Adv. Mater.* **2014**, *26*, 10-28.
- (4) Zhu, X. Y.; Monahan, N. R.; Gong, Z. Z.; Zhu, H. M.; Williams, K. W.; Nelson, C. A. Charge Transfer Excitons at van der Waals Interfaces. *J. Am. Chem. Soc.* **2015**, *137*, 8313-8320.
- (5) Ostroverkhova, O. Organic Optoelectronic Materials: Mechanisms and Applications. *Chem. Rev.* **2016**, *116*, 13279-13412.
- (6) Ponseca, C. S.; Chabera, P.; Uhlig, J.; Persson, P.; Sundstrom, V. Ultrafast Electron Dynamics in Solar Energy Conversion. *Chem. Rev.* **2017**, *117*, 10940-11024.
- (7) Ye, Z. L.; Cao, T.; O'Brien, K.; Zhu, H. Y.; Yin, X. B.; Wang, Y.; Louie, S. G.; Zhang, X. Probing excitonic dark states in single-layer tungsten disulphide. *Nature* **2014**, *513*, 214-218.
- (8) He, K. L.; Kumar, N.; Zhao, L.; Wang, Z. F.; Mak, K. F.; Zhao, H.; Shan, J. Tightly Bound Excitons in Monolayer WSe2. *Phys. Rev. Lett.* **2014**, *113*, 026803.
- (9) Scholes, G. D.; Rumbles, G. Excitons in nanoscale systems. *Nat. Mater.* **2006**, *5*, 683-696.
- (10) Grancini, G.; Maiuri, M.; Fazzi, D.; Petrozza, A.; Egelhaaf, H. J.; Brida, D.; Cerullo, G.; Lanzani, G. Hot exciton dissociation in polymer solar cells. *Nat. Mater.* **2013**, *12*, 29-33.
- (11) Jailaubekov, A. E.; Willard, A. P.; Tritsch, J. R.; Chan, W. L.; Sai, N.; Gearba, R.; Kaake, L. G.; Williams, K. J.; Leung, K.; Rossky, P. J.; Zhu, X. Y. Hot charge-transfer excitons set the time limit for charge separation at donor/acceptor interfaces in organic photovoltaics. *Nat. Mater.* **2013**, *12*, 66-73.
- (12) Savoie, B. M.; Rao, A.; Bakulin, A. A.; Gelinas, S.; Movaghar, B.; Friend, R. H.; Marks, T. J.; Ratner, M. A. Unequal Partnership: Asymmetric Roles of Polymeric Donor and Fullerene Acceptor in Generating Free Charge. *J. Am. Chem. Soc.* **2014**, *136*, 2876-2884.
- (13) Gelinas, S.; Rao, A.; Kumar, A.; Smith, S. L.; Chin, A. W.; Clark, J.; van der Poll, T. S.; Bazan, G. C.; Friend, R. H. Ultrafast Long-Range Charge Separation in Organic Semiconductor Photovoltaic Diodes. *Science* **2014**, *343*, 512-516.
- (14) Devizis, A.; De Jonghe-Risse, J.; Hany, R.; Nuesch, F.; Jenatsch, S.; Gulbinas, V.; Moser, J. E. Dissociation of Charge Transfer States and Carrier Separation in Bilayer Organic Solar Cells: A Time-Resolved Electroabsorption Spectroscopy Study. *J. Am. Chem. Soc.* **2015**, *137*, 8192-8198.
- (15) Barker, A. J.; Chen, K.; Hodgkiss, J. M. Distance Distributions of Photogenerated Charge Pairs in Organic Photovoltaic Cells. *J. Am. Chem. Soc.* **2014**, *136*, 12018-12026.
- (16) Pensack, R. D.; Guo, C. H.; Vakhshouri, K.; Gomez, E. D.; Asbury, J. B. Influence of Acceptor Structure on Barriers to Charge Separation in Organic Photovoltaic Materials. *J. Phys. Chem. C* **2012**, *116*, 4824-4831.
- (17) Kaake, L. G.; Moses, D.; Heeger, A. J. Charge transfer from delocalized excited states in a bulk heterojunction material. *Phys. Rev. B* **2015**, *91*, 075436.
- (18) Wang, T.; Kafle, T. R.; Kattel, B.; Chan, W.-L. A Multidimensional View of Charge Transfer Excitons at Organic Donor–Acceptor Interfaces. *J. Am. Chem. Soc.* **2017**, *139*, 4098-4106.

- (19) McMahon, D. P.; Cheung, D. L.; Troisi, A. Why Holes and Electrons Separate So Well in Polymer/Fullerene Photovoltaic Cells. *J. Phys. Chem. Lett.* **2011**, *2*, 2737-2741.
- (20) Groves, C. Suppression of geminate charge recombination in organic photovoltaic devices with a cascaded energy heterojunction. *Energy Environ Sci* **2013**, *6*, 1546-1551.
- (21) Bartelt, J. A.; Beiley, Z. M.; Hoke, E. T.; Mateker, W. R.; Douglas, J. D.; Collins, B. A.; Tumbleston, J. R.; Graham, K. R.; Amassian, A.; Ade, H.; Frechet, J. M. J.; Toney, M. F.; McGehee, M. D. The Importance of Fullerene Percolation in the Mixed Regions of Polymer-Fullerene Bulk Heterojunction Solar Cells. *Adv Energy Mater* **2013**, *3*, 364-374.
- (22) Westacott, P.; Tumbleston, J. R.; Shoaee, S.; Fearn, S.; Bannock, J. H.; Gilchrist, J. B.; Heutz, S.; deMello, J.; Heeney, M.; Ade, H.; Durrant, J.; McPhail, D. S.; Stingelin, N. On the role of intermixed phases in organic photovoltaic blends. *Energy Environ Sci* **2013**, *6*, 2756-2764.
- (23) Burke, T. M.; McGehee, M. D. How High Local Charge Carrier Mobility and an Energy Cascade in a Three-Phase Bulk Heterojunction Enable > 90% Quantum Efficiency. *Adv. Mater.* **2014**, *26*, 1923-1928.
- (24) Shi, L.; Lee, C. K.; Willard, A. P. The Enhancement of Interfacial Exciton Dissociation by Energetic Disorder Is a Nonequilibrium Effect. *Acs Central Sci* **2017**, *3*, 1262-1270.
- (25) D'Avino, G.; Muccioli, L.; Olivier, Y.; Beljonne, D. Charge Separation and Recombination at Polymer-Fullerene Heterojunctions: Delocalization and Hybridization Effects. *J. Phys. Chem. Lett.* **2016**, *7*, 536-540.
- (26) Ceballos, F.; Ju, M. G.; Lane, S. D.; Zeng, X. C.; Zhao, H. Highly Efficient and Anomalous Charge Transfer in van der Waals Trilayer Semiconductors. *Nano Lett.* **2017**, *17*, 1623-1628.
- (27) Mueller, C. J.; Brendel, M.; Ruckdeschel, P.; Pflaum, J.; Thelakkat, M. Diketopyrrolopyrroles with a Distinct Energy Level Cascade for Efficient Charge Carrier Generation in Organic Solar Cells. *Adv Energy Mater* **2015**, *5*, 1500914.
- (28) Nakano, K.; Suzuki, K.; Chen, Y. J.; Tajima, K. Roles of Energy/Charge Cascades and Intermixed Layers at Donor/Acceptor Interfaces in Organic Solar Cells. *Sci. Rep.* **2016**, *6*, 29529.
- (29) Tan, Z. K.; Johnson, K.; Vaynzof, Y.; Bakulin, A. A.; Chua, L. L.; Ho, P. K. H.; Friend, R. H. Suppressing Recombination in Polymer Photovoltaic Devices via Energy-Level Cascades. *Adv. Mater.* **2013**, *25*, 4131-4138.
- (30) Xu, H. J.; Ohkita, H.; Tamai, Y.; Benten, H.; Ito, S. Interface Engineering for Ternary Blend Polymer Solar Cells with a Heterostructured Near-IR Dye. *Adv. Mater.* **2015**, *27*, 5868-5874.
- (31) Kinoshita, Y.; Hasobe, T.; Murata, H. Control of open-circuit voltage in organic photovoltaic cells by inserting an ultrathin metal-phthalocyanine layer. *Appl. Phys. Lett.* **2007**, *91*.
- (32) Kafle, T. R.; Chan, W. L. Exciton Heating Versus Cooling: Charge Separation Driven by Entropy and Delocalization at Interfaces with Planar Molecules. *Phys. Rev. Appl.* **2021**, *15*, 044054.
- (33) Kafle, T. R.; Kattel, B.; Wanigasekara, S.; Wang, T.; Chan, W. L. Spontaneous Exciton Dissociation at Organic Semiconductor Interfaces Facilitated by the Orientation of the Delocalized Electron-Hole Wavefunction. *Adv Energy Mater* **2020**, *10*, 1904013.
- (34) Rijal, K.; Rudayni, F.; Kafle, T. R.; Chan, W.-L. Collective Effects of Band Offset and Wave Function Dimensionality on Impeding Electron Transfer from 2D to Organic Crystals. *J. Phys. Chem. Lett.* **2020**, *11*, 7495-7501.
- (35) Kattel, B.; Qin, L.; Kafle, T. R.; Chan, W. L. Graphene Field-Effect Transistor as a High-Throughput Platform to Probe Charge Separation at Donor-Acceptor Interfaces. *J. Phys. Chem. Lett.* **2018**, *9*, 1633-1641.

- (36) Kafle, T. R.; Kattel, B.; Wang, T.; Chan, W.-L. The relationship between the coherent size, binding energy and dissociation dynamics of charge transfer excitons at organic interfaces. *J. Phys.: Condens. Matter* **2018**, *30*, 454001.
- (37) Wang, T.; Kafle, T. R.; Kattel, B.; Liu, Q. F.; Wu, J.; Chan, W. L. Growing Ultra-flat Organic Films on Graphene with a Face-on Stacking via Moderate Molecule-Substrate Interaction. *Sci. Rep.* **2016**, *6*, 28895.
- (38) Gao, W. Y.; Kahn, A. Electronic structure and current injection in zinc phthalocyanine doped with tetrafluorotetracyanoquinodimethane: Interface versus bulk effects. *Org. Electron.* **2002**, *3*, 53-63.
- (39) Martinez-Galera, A. J.; Nicoara, N.; Martinez, J. I.; Dappe, Y. J.; Ortega, J.; Gomez-Rodriguez, J. M. Imaging Molecular Orbitals of PTCDA on Graphene on Pt(111): Electronic Structure by STM and First-Principles Calculations. *J. Phys. Chem. C* **2014**, *118*, 12782-12788.
- (40) Konstantatos, G.; Badioli, M.; Gaudreau, L.; Osmond, J.; Bernechea, M.; de Arquer, F. P. G.; Gatti, F.; Koppens, F. H. L. Hybrid graphene-quantum dot phototransistors with ultrahigh gain. *Nat. Nanotechnol.* **2012**, *7*, 363-368.
- (41) Koppens, F. H. L.; Mueller, T.; Avouris, P.; Ferrari, A. C.; Vitiello, M. S.; Polini, M. Photodetectors based on graphene, other two-dimensional materials and hybrid systems. *Nat. Nanotechnol.* **2014**, *9*, 780-793.
- (42) Qin, L.; Wu, L. P.; Kattel, B.; Li, C. H.; Zhang, Y.; Hou, Y. B.; Wu, J.; Chan, W. L. Using Bulk Heterojunctions and Selective Electron Trapping to Enhance the Responsivity of Perovskite-Graphene Photodetectors. *Adv. Funct. Mater.* **2017**, *27*, 1704173.
- (43) Wang, T.; Chan, W. L. Dynamical Localization Limiting the Coherent Transport Range of Excitons in Organic Crystals. *J. Phys. Chem. Lett.* **2014**, *5*, 1812-1818.
- (44) Wang, T.; Kafle, T. R.; Kattel, B.; Chan, W. L. Observation of an Ultrafast Exciton Hopping Channel in Organic Semiconducting Crystals. *J. Phys. Chem. C* **2016**, *120*, 7491-7499.
- (45) Castro, E. V.; Novoselov, K. S.; Morozov, S. V.; Peres, N. M. R.; Dos Santos, J. M. B. L.; Nilsson, J.; Guinea, F.; Geim, A. K.; Castro Neto, A. H. Biased bilayer graphene: Semiconductor with a gap tunable by the electric field effect. *Phys. Rev. Lett.* **2007**, *99*, 216802.
- (46) Zhang, Y. B.; Tang, T. T.; Girit, C.; Hao, Z.; Martin, M. C.; Zettl, A.; Crommie, M. F.; Shen, Y. R.; Wang, F. Direct observation of a widely tunable bandgap in bilayer graphene. *Nature* **2009**, *459*, 820-823.
- (47) Katsidis, C. C.; Siapkas, D. I. General transfer-matrix method for optical multilayer systems with coherent, partially coherent, and incoherent interference. *Appl. Opt.* **2002**, *41*, 3978-3987.
- (48) Byrnes, S. J. Multilayer optical calculations **2016**, arXiv:1603.02720v2.
- (49) Brendel, M.; Krause, S.; Steindamm, A.; Topczak, A. K.; Sundarraj, S.; Erk, P.; Hohla, S.; Fruehauf, N.; Koch, N.; Pflaum, J. The Effect of Gradual Fluorination on the Properties of FnZnPc Thin Films and FnZnPc/C-60 Bilayer Photovoltaic Cells. *Adv. Funct. Mater.* **2015**, *25*, 1565-1573.
- (50) Liang, X. L.; Sperling, B. A.; Calizo, I.; Cheng, G. J.; Hacker, C. A.; Zhang, Q.; Obeng, Y.; Yan, K.; Peng, H. L.; Li, Q. L.; Zhu, X. X.; Yuan, H.; Walker, A. R. H.; Liu, Z. F.; Peng, L. M.; Richter, C. A. Toward Clean and Crackless Transfer of Graphene. *ACS Nano* **2011**, *5*, 9144-9153.
- (51) Giovannetti, G.; Brocks, G.; van den Brink, J. Ab initio electronic structure and correlations in pristine and potassium-doped molecular crystals of copper phthalocyanine. *Phys. Rev. B* **2008**, 77, 035133.

- (52) Saito, S.; Oshiyama, A. Cohesive Mechanism and Energy-Bands of Solid C60. *Phys. Rev. Lett.* **1991**, *66*, 2637-2640.
- (53) Jiang, H.; Ye, J.; Hu, P.; Wei, F. X.; Du, K. Z.; Wang, N.; Ba, T.; Feng, S. L.; Kloc, C. Fluorination of Metal Phthalocyanines: Single-Crystal Growth, Efficient N-Channel Organic Field-Effect Transistors, and Structure-Property Relationships. *Sci. Rep.* **2014**, *4*, 7573.
- (54) Norton, J. E.; Bredas, J. L. Theoretical characterization of titanyl phthalocyanine as a ptype organic semiconductor: Short intermolecular pi-pi interactions yield large electronic couplings and hole transport bandwidths. *J. Chem. Phys.* **2008**, *128*, 034701.